frontiers | Frontiers in Environmental Science

TYPE Original Research
PUBLISHED 23 October 2024
DOI 10.3389/fenvs.2024.1482113



OPEN ACCESS

EDITED BY
Arindam Malakar,
University of Nebraska-Lincoln, United States

REVIEWED BY
Sudipta Rakshit,
Tennessee State University, United States
Yun Liu,
Chinese Academy of Sciences (CAS), China

*CORRESPONDENCE
Changwei Lü,
lcw2008@imu.edu.cn
Jiang He,
ndjhe@imu.edu.cn

RECEIVED 17 August 2024
ACCEPTED 15 October 2024
PUBLISHED 23 October 2024

CITATION
Li H, Song W, Li Z, Wang W, He J and Lü C (2024) Adsorption characteristics of As(III) by schwertmannite: new findings in mineral-phase transformation and microbial effects. *Front. Environ. Sci.* 12:1482113. doi: 10.3389/fenvs.2024.1482113



# Adsorption characteristics of As(III) by schwertmannite: new findings in mineral-phase transformation and microbial effects

Hao Li[1], Wenjie Song[2], Zhichao Li[1], Wei Wang[1,3], Jiang He[1,3]* and Changwei Lü[1,3]*

[1]School of Ecology and Environment, Inner Mongolia University, Hohhot, China, [2]Pioneer College, Inner Mongolia University, Hohhot, China, [3]Institute of Environmental Geology, Inner Mongolia University, Hohhot, China

The amount of As(III) adsorbed and the interfacial process are closely associated with the phase transformation of Schwertmannite (SCH). At present, studies on the adsorption characteristics of As(III) on SCH and the accompanying phase transformation process, especially the related mechanisms under the mediation of iron-reducing bacteria (FeRB) and sulfate-reducing bacteria (SRB), are limited in existing literature. With the help of continuous characterization, the adsorption behavior of As(III) on SCH was explored, as well as the transformation processes of SCH during these processes. The findings revealed that the SCH, synthesized by the $KMnO_4$ oxidation and ethanol modification methods, exhibited excellent physical adsorption capacity for As(III) due to their increasing specific surface area and porosity. At room temperature (20°C), the saturation adsorption capacities of As(III) by M-SCH and Y-SCH reached 62.69 and 58.62 mg/g, respectively. Moreover, the generation and phase transformation of As(III)-bearing ferrihydrite were observed within a 60-min timeframe. It is the first time this phenomenon has been observed in such a short time, which is presumed to be an intermediate stage in the transformation of SCH into goethite. Furthermore, both FeRB and SRB could enhance the adsorption capacity of SCH for As(III). Comparatively, SRB has a more substantial impact on SCH's phase transformation. These insights are valuable for the practical application of SCH in treating As(III) pollution.

KEYWORDS

**schwertmannite, As(III), adsorption characteristics, phase transformation, microbial influence**

## 1 Introduction

Arsenic (As), a toxic and carcinogenic metalloid, is widely distributed in the natural environment (Oremland and Stolz, 2003). The bioavailability, toxicity, migration, and transformation of As are species-dependent (Oremland and Stolz, 2003; Chen and Rosen, 2020). As primarily occurs in two oxidation states: arsenite (As(III)) and arsenate (As(V)), with As(III) exhibiting greater biological toxicity and mobility compared to As(V) (Oremland and Stolz, 2003). Studies have indicated that the concentration of As(III) in severe acid mine drainage (AMD) can reach as high as 0.35–12.15 g/L (Morin et al., 2003;

Yuan et al., 2021). Additionally, As(III) concentrations ranging from 2.5 to 846 μg/L and 5.6 to 2,680 μg/L have been detected in groundwater samples from Bangladesh and the Datong Basin in China, respectively (Ahmed et al., 2004; Pi et al., 2015). Given the higher toxicity and mobility of As(III), contamination in both surface water and groundwater requires significant attention.

Schwertmannite (SCH), a poorly crystalline Fe(III) oxyhydroxy-sulfate mineral, is commonly found in AMD and acidic sulfate soils (Bigham et al., 1994; Schoepfer and Burton, 2021), presenting notable adsorption ability due to its large surface area and abundance of surface hydroxyl groups (-OH) (Schoepfer and Burton, 2021). Previous studies have shown that the saturated adsorption capacity of synthesized SCH for As(III) at room temperature ranges from 19.9 to 217.9 mg/g (Burton et al., 2009; Song et al., 2015; Lee et al., 2023). SCH exhibits high adsorption capacity for As(III) across a broad pH range, outperforming other iron-based adsorption materials such as iron oxide-coated geopolymers and $Fe_3O_4$-graphene (Guo et al., 2015; Thakur and Armstrong, 2021). Furthermore, the presence of coexisting ions and dissolved organic matter has minimal impact on SCH's adsorption capacity for As (Dou et al., 2013). Consequently, SCH is considered a promising mineral adsorbent for As(III) removal from aqueous environments (Schoepfer and Burton, 2021). The potential applications and optimization of SCH for As(III) remediation have been extensively investigated (Cao et al., 2021; Zhang D. et al., 2022; Wang X. et al., 2023). For instance, using $KMnO_4$ instead of the conventional oxidant $H_2O_2$ in SCH preparation has shown promise in enhancing SCH's adsorption capacity for As(V) (Cao et al., 2021). Additionally, ethanol modification has been employed to introduce more -OH groups into SCH, thereby increasing its adsorption capacity for As(III) (Zhang D. et al., 2022). Despite these advancements, existing literature primarily focuses on enhancing SCH's adsorption capacity for As(III) through individual optimized synthesis methods, lacking comparative studies of different optimization techniques. Comparing the adsorption mechanisms of SCHs prepared by various methods for As(III) offers a promising approach to identify effective strategies for As(III) removal.

SCH is inherently unstable and gradually transforms into minerals such as goethite, lepidocrocite, and jarosite (Vithana et al., 2015; Xie et al., 2017; Wang et al., 2020; Naren et al., 2023). The transformation of SCH is influenced by its structural composition and environmental conditions (Schoepfer and Burton, 2021), then inevitably impacting SCH's adsorption capacity. Studies on SCH's long-term phase transformations have been extensively conducted at the resolution in days, there are few investigations on the short-term SCH phase transformations during its quick adsorption of As(III) (24 h), particularly under the influence of iron-reducing bacteria (FeRB) and sulfate-reducing bacteria (SRB) (Johnston et al., 2011; Fan et al., 2019; Chen et al., 2020). FeRB and SRB are prevalent in natural environments, and their metabolic activities are closely linked to SCH's transformation and As(III) migration (Schoepfer and Burton, 2021; Shi et al., 2021; Gao et al., 2022). Investigating the effects of FeRB and SRB on SCH's interaction with As(III) is crucial for advancing the practical utilization of SCH.

This study employed two optimized chemical oxidation methods to synthesize two types of SCH. Batch adsorption experiments were then conducted to examine the adsorption of As(III) by these SCHs. The primary objectives of this study are: 1) to compare the differences in adsorption capacity and mechanisms of the optimized SCHs for As(III), 2) to investigate the impact of FeRB and SRB on the adsorption behavior of As(III) on SCH, and 3) to elucidate the phase transformation of SCH during the short-term adsorption process (0–24 h), particularly under the mediation of FeRB and SRB. This work provides a deeper understanding of the intermediate adsorption process of As(III) by SCH, offering valuable insights for the practical application of SCH in treating As(III) pollution.

# 2 Materials and methods

## 2.1 SCH synthesis

H-SCH was synthesized via $H_2O_2$ oxidation method as described by Regenspurg et al. (Regenspurg et al., 2004). Briefly, 5.56 g of $FeSO_4.7H_2O$ was dissolved in 248 mL ultrapure water. Then, 2 mL of 30% $H_2O_2$ was added slowly and uniformly while stirring for 2 min (min). The resulting precipitate was incubated for 24 h (h) in a constant temperature shaker at 180 rpm and 25°C. The synthesized H-SCH was then filtered through a 0.45 μm filter and rinsed with deionized water more than five times until the pH value of the solution used to rinse SCH stabilized. Subsequently, the H-SCH was filtered again using a 0.45 μm filter and dried at 60 °C for 12 h. The dried SCH was then ground and passed through a 150-mesh sieve.

M-SCH was synthesized using the $KMnO_4$ oxidation method, optimized from the $H_2O_2$ oxidation method, as described by Cao et al. (Cao et al., 2021). In this method, 0.3 g of $KMnO_4$ replaced $H_2O_2$, with all other steps remaining the same as for H-SCH.

Y-SCH was synthesized using an ethanol modification method, optimized from the $H_2O_2$ oxidation method, as described by Zhang et al. (Zhang D. et al., 2022). Here, 248 mL of 20% ethanol solution replaced ultrapure water, with all other steps remaining the same as for H-SCH. The rate of adding the oxidant in the preparation of H-SCH, M-SCH, and Y-SCH was consistent.

## 2.2 Adsorption kinetics and isotherms

To investigate the adsorption capacity and mechanism of SCH for As(III), batch experiments of adsorption kinetics and isothermal adsorption were conducted in the 50 mL centrifuge tubes containing 40 mL 0.001M NaCl electrolyte (pH 7) with 1.5 g/L SCHs. In the adsorption kinetics experiment, the time intervals were 5, 15, 30, 60, 120, 240, 360, 480, 720, 1,440 and 2,880 min, respectively, with an initial As(III) concentration of 100 mg/L at 20 °C. According to the results of adsorption kinetics experiment, the equilibrium time was set at 1,440 min for the isothermal adsorption experiments. To obtain the thermodynamic parameters and saturation adsorption capacity of SCH for As(III), isothermal adsorption experiments were conducted at temperatures of 20, 30, and 40°C, with initial As(III) concentration from 10 to 350 mg/L. All experiments were carried out in a thermostatic water bath oscillator at 180 rpm and triplicated. At the end of each experiment, supernatants and solids were

obtained by centrifugation, respectively. The concentrations of As(III) and total Fe in the liquid samples were analyzed after passing through a 0.22 μm filter. To obtain a completely dry SCH sample, the collected SCHs were dried at 35°C for 48 h, and then fully ground for subsequent characterizations (Zhang D. et al., 2022; Wang X. M. et al., 2023). Before use, all laboratory glassware was soaked in 5% (v/v) $HNO_3$ solutions for at least 24 h, followed by repeated rinsing with deionized water (Milli-Q). All reagents used were analytical grade in this study.

## 2.3 The impact of microorganisms

*Shewanella oneidensis strain MR-1* (MR-1) and *Desulfovibrio desulfuricans subsp.desulfuricans* (referred to as SRB hereafter) were selected in this study. The detailed bacteria culture conditions for MR-1 and SRB can be found in the Supplementary Text S1. All experimental vessels were sterilized by autoclaving and UV sterilization, and all experimental procedures were conducted in an anaerobic sterile glove box. The impact experiments of MR-1 and SRB were divided into two distinct groups: experimental (B and C groups) and control group (A group). The experimental group involved the addition of either MR-1 or SRB to investigate their effect on the adsorption process, while the control group was without the addition of MR-1 or SRB. Each group was conducted in the 50 mL centrifuge tubes, and As(III) solution prepared with sterilized deoxygenated ultra-pure water and SCH was added in a 50 mL centrifuge tube to reach a 40 mL system with 50 mg/L A(III) and 1.5 g/L SCH. The bacterial concentration of experimental group was $2\times10^8$ cells/mL, and DL-sodium lactate (50 mM) was introduced as the carbon source. Each group was performed in triplicates, and the incubation period lasted for 24 h at 20 °C. At the end of each experiment, supernatants and solids were obtained by centrifugation. The concentrations of As(III), total Fe and Fe(II) in the liquid samples were analyzed after passing through a 0.22 μm filter. The collected SCHs were dried at 35°C for 48 h, and then fully ground for subsequent characterizations (Zhang D. et al., 2022; Wang X. M. et al., 2023).

## 2.4 Analytical methods

The concentrations of total Fe and Fe(II) were analyzed by the 1,10-phenanthroline method (Gao et al., 2022) (UV-2550, Shimadzu, Japan). The concentration of As(III) was analyzed by atomic fluorescence spectroscopy (HG-AFS 3100, Beijing Created High-Guarantee Instrumentation, China), detailed testing methods are provided in Supplementary Text S3. The X-ray diffraction (XRD) patterns were recorded on a Bruker D8 Advance diffractometer (Germany) using Cu Kα radiation (40 kV, 30 mA, 0.1 s/step), and the data of the crystallite phase were taken in 2-theta from 15° to 80°. Fourier transform infrared (FTIR) spectroscopy was conducted with an IRTRACER-100 (Shimadzu, Japan) with the following settings: attenuated total reflection (ATR) mode, scanned in the wavenumber range of 4,000 $cm^{-1}$–400 $cm^{-1}$, with a resolution of 4 $cm^{-1}$. X-ray photoelectron spectroscopy (XPS) was conducted on an ESCALABXI + spectrometer (Thermo Fisher, USA) with monochromatized Al Kα radiation and the binding energy positions were calibrated against C1s at 284.8 eV. Scanning electron microscopy with energy dispersive spectroscopy (SEM-EDS) was conducted on an S-4800 scanning electron microscope (HITACHI, Japan). The specific surface area and pore volume were calculated based on the Brunauer-Emmett-Teller method (ASAP2020, Micromeritics, US).

The infrared peak area (IPA) of SCHs was calculated by curve integral in Origin 2021 (Li et al., 2018; Li et al., 2021). XPS data was drawn through Avantage 5.9931. Other pictures and data analysis were completed through Origin 2021 and Excel 2021.

# 3 Results and discussion

## 3.1 Characterization of morphology and structural composition

The XRD pattern of H-SCH, M-SCH and Y-SCH (SCHs) exhibited eight characteristic peaks that matches the SCH standard PDF pattern (PDF: 47–1775) (Figure 1A). The XRD spectra of SCH in the existing literature are similar to the amorphous peaks observed in this study, which is due to SCH being a poorly crystalline iron hydroxyl sulfate mineral (Chen et al., 2020; Wang et al., 2020; Cao et al., 2021; Jia et al., 2024). The FTIR results (Figure 1B) indicated that the functional groups of the studied SCHs (H-SCH, M-SCH, and Y-SCH) were consistent with spectra in the literature, including surface -OH groups (3,206 $cm^{-1}$), outer-sphere $SO_4^{2-}$ (1,087 and 977 $cm^{-1}$), structural $SO_4^{2-}$ (605 $cm^{-1}$), as well as Fe-O (694 $cm^{-1}$) groups (Peak et al., 1999; Paikaray et al., 2012; Chen et al., 2022; Tian et al., 2023). These alignments confirmed the successful synthesis of SCHs using various methods (Vithana et al., 2014; Cao et al., 2021; Zhang D. et al., 2022; Naren et al., 2023). However, notable distinctions were observed in terms of elemental composition, functional group content, and surface morphology among the three types of SCHs. Differences in infrared peak area (IPA), representing different function group content, were observed among the synthesized SCHs (Supplementary Table S1) (Brülls et al., 2007; Li et al., 2018; Wieser et al., 2022). Both M-SCH and Y-SCH exhibited higher content of $SO_4^{2-}$ and -OH. Additionally, EDS results (Supplementary Figure S1) and elemental composition analysis (Supplementary Table S2) confirmed that M-SCH and Y-SCH contained more sulfur, consistent with the higher content of $SO_4^{2-}$ in these samples. The surface of H-SCH was relatively smooth (Supplementary Figure S1), while M-SCH and Y-SCH had uneven wrinkles, with Y-SCH displaying a wool ball-like structure. This uneven surface morphology contributed to an increased specific surface area and average pore volume of M-SCH and Y-SCH (Supplementary Table S3). These results indicated that compared to the $H_2O_2$ oxidation method, the $KMnO_4$ oxidation (M-SCH) and ethanol modification (Y-SCH) methods enhanced the structural properties of SCH.

## 3.2 Kinetics and isothermal adsorption

Previous studies have shown that the adsorption of As(III) by SCH is often accompanied by the oxidation of As(III), with the

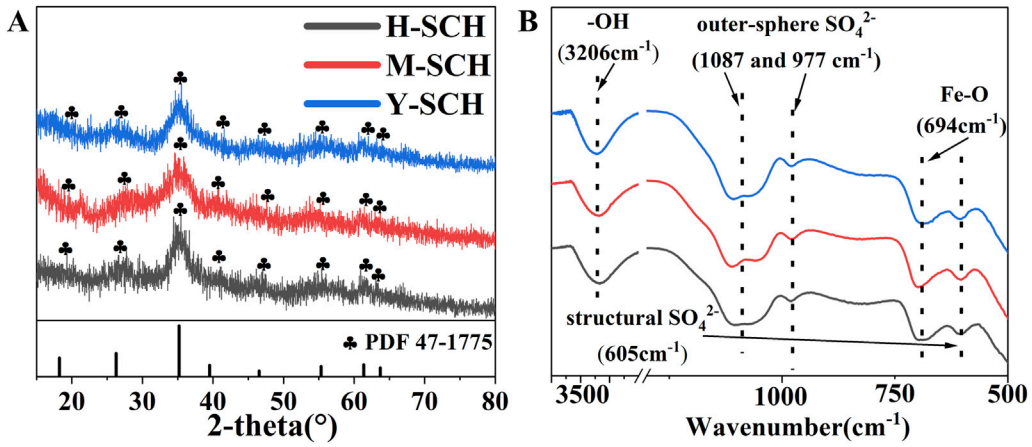


FIGURE 1
Structure and composition characteristics of SCH. Note: **(A)** X-ray diffraction (XRD) and **(B)** Fourier transform infrared (FTIR) patterns of H-SCH, M-SCH and Y-SCH, PDF 47-1775 is the standard pattern for nature SCH.

oxidation rate related to the As/Fe ratio on the SCH surface (Paikaray et al., 2012). If As(III) oxidation occurs, competitive adsorption between As(III) and As(V) on SCH is expected. Theoretically, As(III) is relatively stable in homogeneous solutions with low oxidation rate by $O_2$ and Fe(III) in water environments (Gulledge and O'Connor, 1973; Oscarson et al., 1980; Zhao Z. et al., 2011). Within the 24 h reaction period in this study, continuous XPS characterization results revealed no peaks corresponding to As(V) and Fe(II) were observed (Supplementary Figure S2; Supplementary Figure S3) (Gan et al., 2015; Fan et al., 2023). This result indicated that $O_2$ and Fe(III) in system did not oxidize As(III) to As(V) in this study. The high concentration of As(III) (100 mg/L) in this system led to a high As/Fe ratio on the SCH surface, inhibiting As(III) oxidation (Burton et al., 2009; Paikaray et al., 2011; 2012).

In this study, all SCH samples reached adsorption equilibrium within 24 h (1,440 min, Supplementary Figure S4). The pseudo-second-order kinetic model (Supplementary, Section S2) provided a better fit for the changes in As(III) concentration, as shown in Supplementary Table S4. Furthermore, the adsorption of As(III) by the investigated SCHs was a spontaneous endothermic reaction ($\Delta G < 0$, $\Delta S > 0$, $\Delta H > 0$) (Albadarin et al., 2012), with a slight enhancement in adsorption capacity observed with increasing temperature (Supplementary Figures S5A-F). The adsorption capacity of SCHs for As(III) followed the order Y-SCH > M-SCH > H-SCH at temperatures of 20, 30, and 40 °C. Notably, at room temperature (20 °C), the SCH samples exhibited excellent adsorption capacities for As(III), with Y-SCH at 62.69 mg/g, M-SCH at 58.62 mg/g, and H-SCH at 52.16 mg/g (Supplementary Figures S5A-C). Considering the adsorption capacity for As(III), along with the larger specific surface area and average pore volume of M-SCH and Y-SCH (Supplementary Table S3), Y-SCH and M-SCH exhibit superior performance compared to H-SCH. Therefore, Y-SCH and M-SCH were selected as the focus for further investigation into the adsorption dynamics and the impact of microorganisms.

Typically, the pseudo-second-order kinetic model is used to describe chemical adsorption processes (Ho and McKay, 1999). However, in this work, the calculated $\Delta H$ values for M-SCH and Y-SCH were 10.65 and 30.78 kJ/mol, respectively (Supplementary Table S5; Supplementary Figures S5D-F, see Text S2 for calculation method). The $\Delta H$ for adsorption governed by chemical adsorption ranges between 40 and 120 kJ/mol (Alkan et al., 2004; Zhao D. et al., 2011). Since all $\Delta H$ values for the studied SCHs were less than 40 kJ/mol, this implies that physical adsorption predominantly governs the adsorption of As(III) by SCHs. Therefore, the specific adsorption mechanism between SCHs and As(III) needs further analysis using infrared peak area (IPA) analysis. Figure 2 showed a reduction in the IPA of -OH (3,206 $cm^{-1}$), outer-sphere $SO_4^{2-}$ (1,087 and 977 $cm^{-1}$), and structural $SO_4^{2-}$ (605 $cm^{-1}$) groups. This indicated the involvement of both -OH complexation and $SO_4^{2-}$ exchange (including outer-sphere and structural $SO_4^{2-}$) during the adsorption of As(III) on M-SCH and Y-SCH (Burton et al., 2009; Carrero et al., 2017). However, the reduction in the content of -OH and $SO_4^{2-}$ in M-SCH and Y-SCH was slight (Figures 3A–C). This suggests that -OH complexation and $SO_4^{2-}$ exchange participate in the adsorption process, but they do not play a dominant role (Brülls et al., 2007; Li et al., 2018; Wieser et al., 2022). Additionally, considering the enhanced specific surface area and porosity of M-SCH and Y-SCH (Supplementary Table S3) favor the physical adsorption of As(III), physical adsorption should play a leading role in the adsorption of As(III) by these materials (Li and Wei, 2022). Compared to M-SCH, Y-SCH has a larger specific surface area and porosity, resulting in a stronger adsorption capacity (Supplementary Figure S4; Supplementary Figures S5A-C). These results indicated that the two optimized chemical oxidation methods primarily enhanced the physical adsorption capacity of SCH for As(III).

## 3.3 The generation and transformation of As(III)-bearing ferrihydrite

In the investigation of M-SCH and Y-SCH, the changes in mineral phase during the dynamic adsorption process were sequentially monitored (Figures 4A, B). The XRD spectra of both M-SCH and Y-SCH exhibited new peaks at 2-theta = 30.7° and 41.4° in the initial stage of the process (60 min), indicating the formation

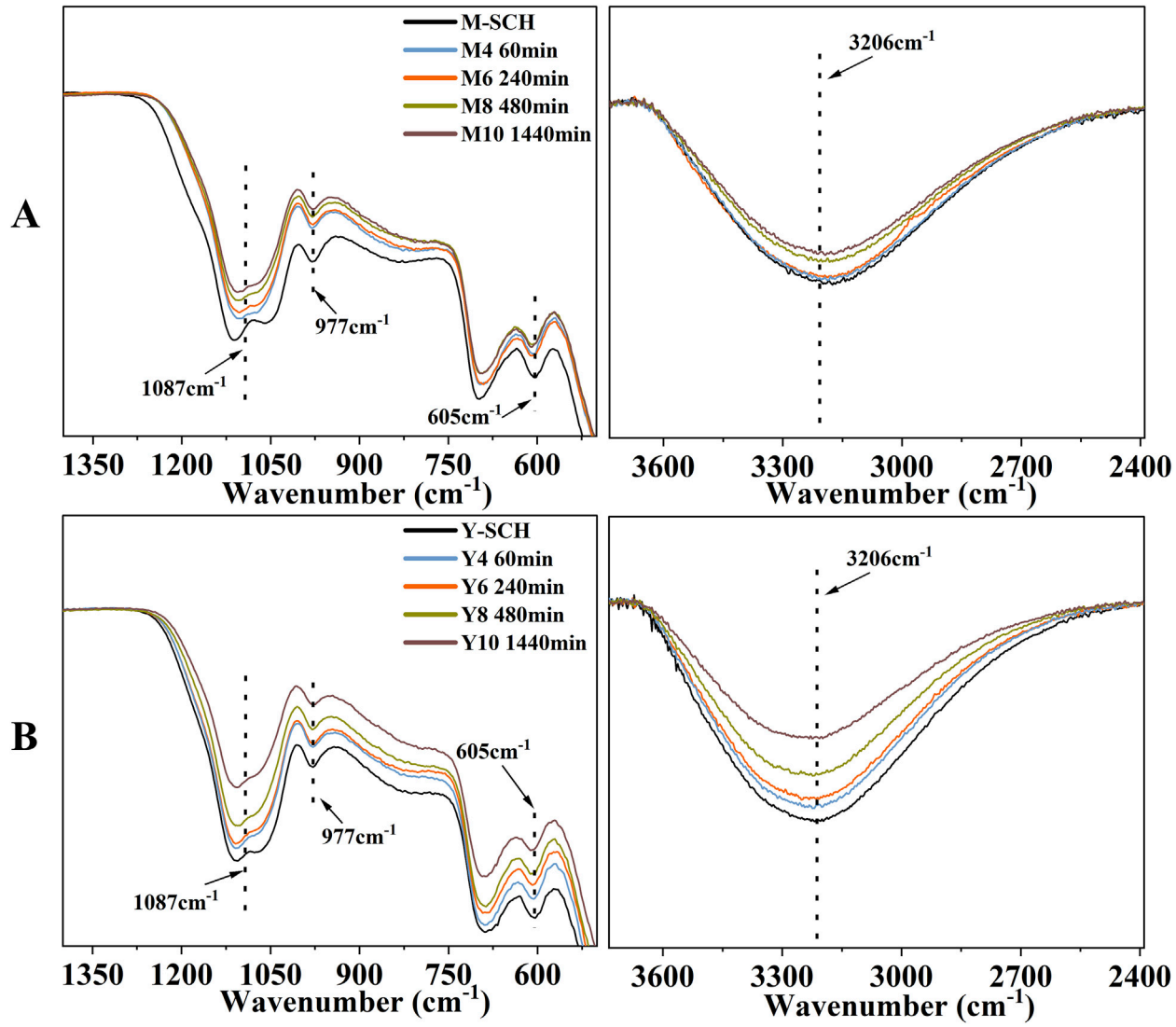


FIGURE 2
The dynamic changes in FTIR spectra during the kinetic process. Note: **(A)** M-SCH and **(B)** Y-SCH.

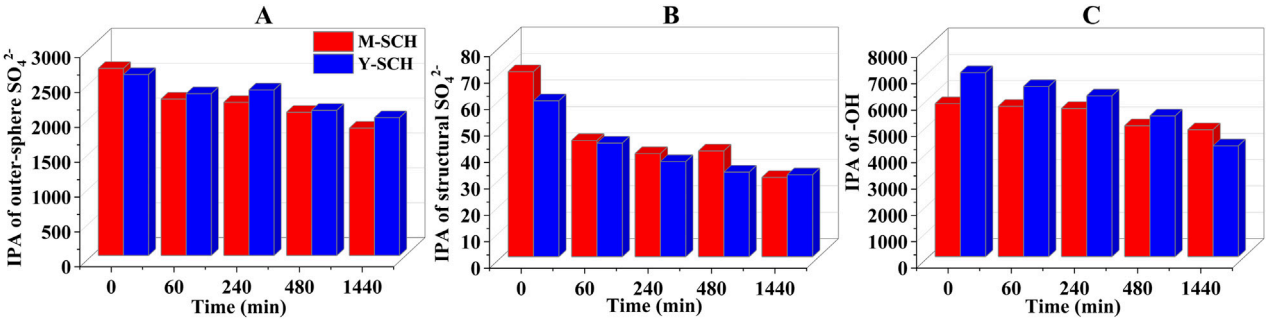


FIGURE 3
Contribution of different functional groups in SCH to As(III) adsorption. Note: **(A)** outer-sphere $SO_4^{2-}$, **(B)** structural $SO_4^{2-}$ and **(C)** surface -OH.

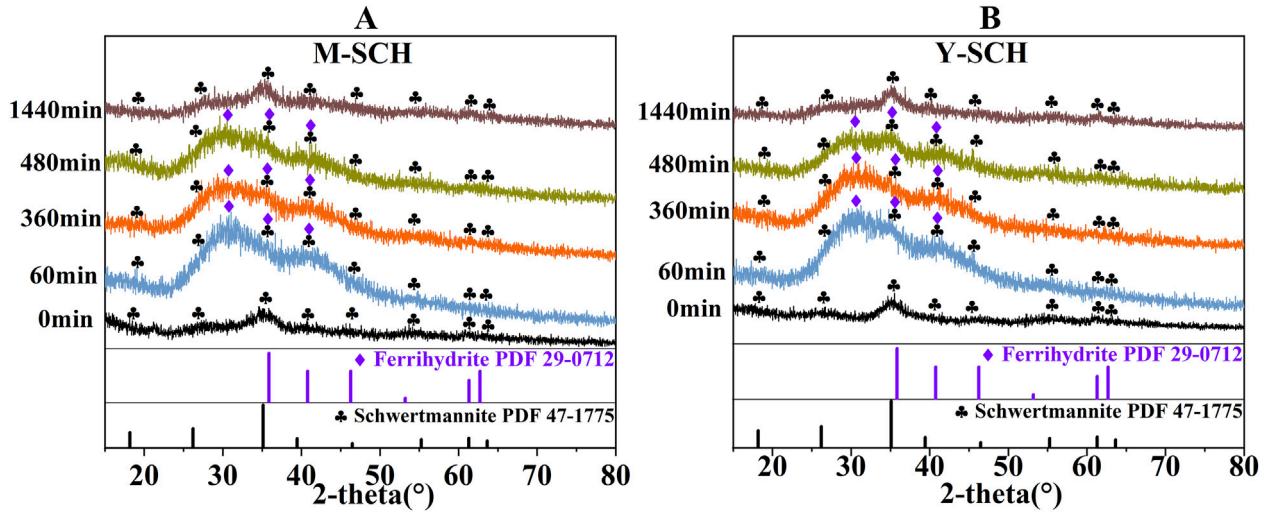


FIGURE 4
The transformation processes of SCH during the kinetic adsorption. Note: **(A)** M-SCH and **(B)** Y-SCH (PDF 47-1775 is the standard pattern for nature SCH, PDF 29-0712 is the standard pattern for ferrihydrite).

of new minerals within the system. Subsequently, the intensity of these peaks gradually diminished over time until they completely disappeared by the end of the process (1,440 min), reverting the system to a mineral composition primarily dominated by SCH. This phenomenon can be explained by the amorphous nature of SCH, which exhibits some solubility in an aqueous environment ($K_{sp}$ = 18.0 ± 2.5) (Burton et al., 2008). Consequently, the dissolution of SCH in water released Fe(III), $SO_4^{2-}$, and $H^+$ ions (Schoepfer and Burton, 2021) (Figures 5A–C). In the presence of As(III), the hydrolysis of Fe(III) led to the formation of As(III)-bearing ferrihydrite through a coprecipitation mechanism (Figure 5D) (Johnston et al., 2011; Yang et al., 2021).

Distinct peaks at 2-theta = 30.7° and 41.4° in Figure 4 correspond to the characteristic peaks of As(III)-bearing ferrihydrite. The deviation of these main XRD peaks from the standard ferrihydrite can be attributed to poor crystallinity induced by the coprecipitation or adsorption of As(III). This causes a shift in the main XRD peaks of standard ferrihydrite from 2-theta = 35.89°, 40.80°, and 46.28° (Figure 4, PDF 29–0712) approximately 5° to the left. Previous studies have also observed that the presence of As(III) leads to a leftward shift in the XRD peaks of ferrihydrite (Takaya et al., 2021). The newly formed As(III)-bearing ferrihydrite exhibited reduced crystallinity and diminished stability, making it susceptible to transformation into alternative mineral phases. Simultaneously, the pH of the aqueous solution continued to decrease due to the release of $H^+$ from the dissolution of SCH (Figure 5B). Additionally, the concentration of released $SO_4^{2-}$ from SCH dissolution and $SO_4^{2-}$ exchange steadily increased. This created an environment of low pH and high $SO_4^{2-}$ concentration conducive to the transformation of As(III)-bearing ferrihydrite into SCH (Ying et al., 2020; Schoepfer and Burton, 2021) (Figures 5A, B). Considering these factors collectively, the newly formed As(III)-bearing ferrihydrite exhibited poor stability and gradually transformed into SCH.

The transformation of As(III)-bearing ferrihydrite to SCH required the utilization of $SO_4^{2-}$ and $H^+$ in the solution (Johnston et al., 2011). However, SCH released $SO_4^{2-}$ during the adsorption of As(III) via $SO_4^{2-}$ exchange, resulting in an unexpected increase in $SO_4^{2-}$ concentration over time (Figure 5A) (Burton et al., 2009; Antelo et al., 2012). Although the change of $SO_4^{2-}$ levels was initially masked, a definitive indication was observed from the pH change (Figure 5B). The pH of M-SCH and Y-SCH systems gradually rose starting at 480 min. This change indirectly confirmed the XRD spectra (Figure 4), indicating the transformation of As(III)-bearing ferrihydrite to SCH after 480 min. This finding differs significantly from the lengthy transformation processes observed in long-term experiments, which can span days, months, or even years. These long-term studies often neglect to monitor SCH during the initial stages of the reaction, particularly within the first 24 h. In such cases, SCH is found to transform directly into goethite over an extended timeframe (Xie et al., 2017; Wang et al., 2020). This study represents the first instance where the generation of As(III)-bearing ferrihydrite was observed, followed by its subsequent transformation into SCH during the short-term (within 24 h) adsorption process between SCH and As(III).

## 3.4 The impact of microorganisms

Figure 6A showed a marked increase in the quantities of Fe(II) in groups supplemented with MR-1 and SRB (B and C groups), compared to groups without these supplements (A group). This increase highlighted the metabolic influence of MR-1 and SRB under the experimental conditions (As(III) concentration = 50 mg/L) (Zhang Z. et al., 2022; Ke et al., 2023). Additionally, Figure 6B demonstrated the ability of MR-1 and SRB to enhance the adsorption capacity of SCH for As(III). It is important to note that this conclusion accounts for the adsorption contributed by the MR-1 and SRB bacteria (Supplementary Figure S6). Compared to MR-1, SRB significantly increased the adsorption of As(III) by SCH. Extracellular polymeric substances (EPS) produced by MR-1 or SRB coated the surface of SCH, aiding in the complexation of As(III) (Ma

10.3389/fenvs.2024.1482113

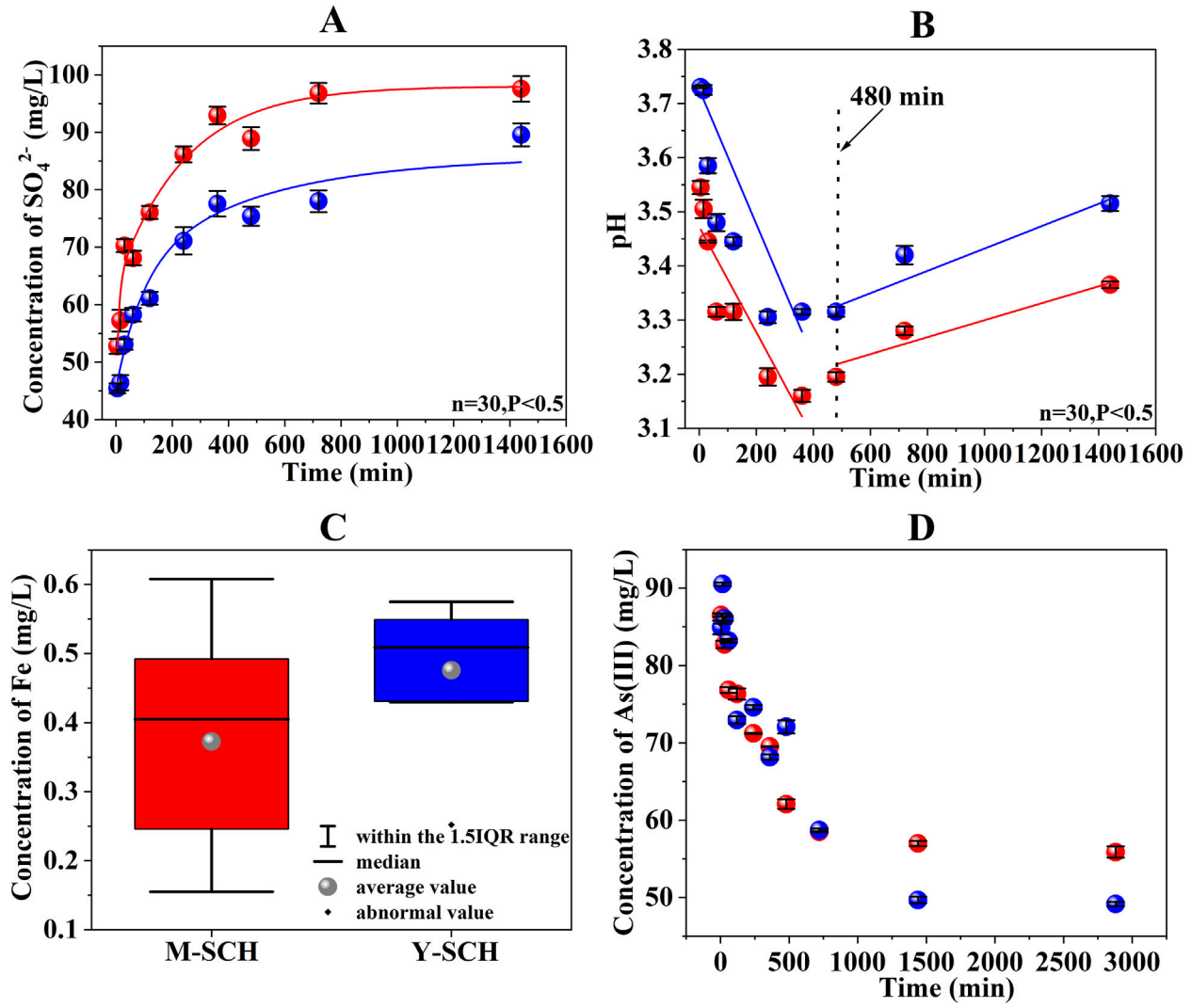


FIGURE 5
The changes in parameters during the kinetic adsorption. Note: **(A)** $SO_4^{2-}$ concentration, **(B)** pH value, **(C)** total Fe concentration in the system solution, and **(D)** As(III) concentration in the system solution (The red in Figure 4 represents the M-SCH data and the blue represents the Y-SCH data).

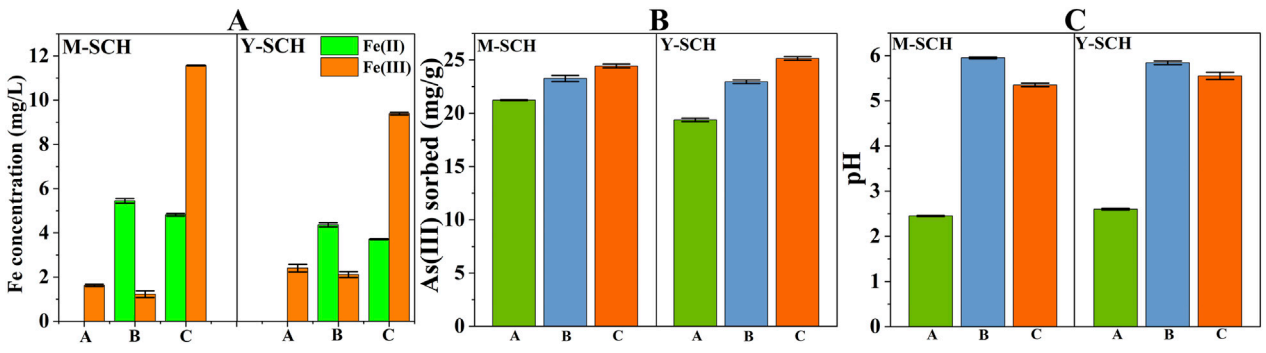


FIGURE 6
The impact of microorganisms on As(III) adsorption by SCH. Note: **(A)** Fe(II) and Fe(III) concentration, **(B)** As(III) adsorption capacity by M-SCH and Y-SCH, **(C)** pH in systems; **(A)** system with only SCH, **(B)** system with SCH and MR-1, **(C)** system with SCH and SRB.

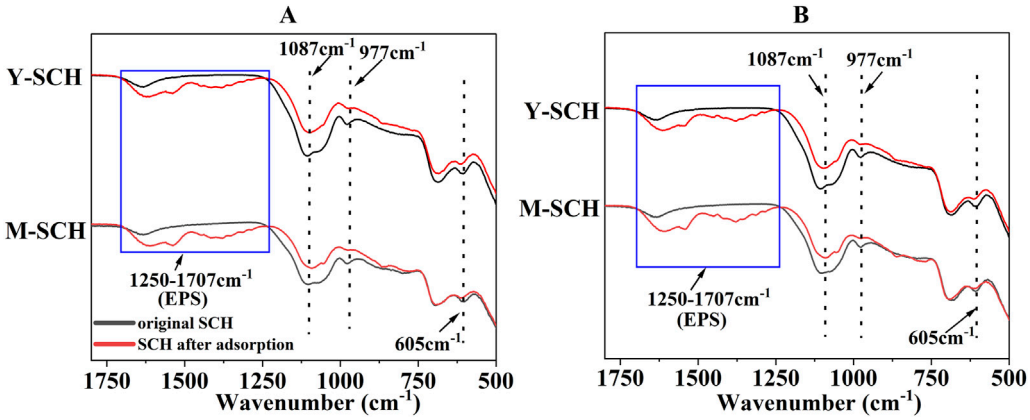


FIGURE 7
The adsorption of extracellular polymeric substances (EPS) on SCH's surface. Note: **(A)** SCH + MR-1 **(B)** SCH + SRB.

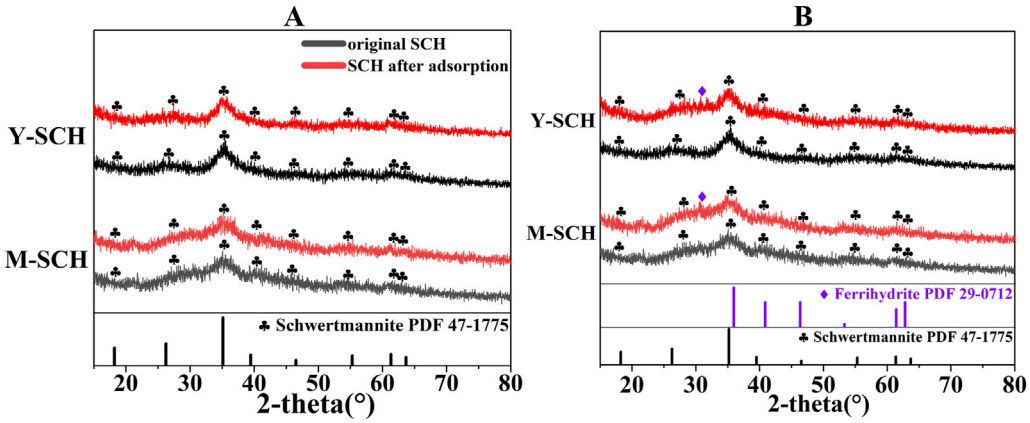


FIGURE 8
The influence of microorganisms on the transformation of SCH. Note: **(A)** SCH + MR-1 **(B)** SCH + SRB. (PDF 47-1775 is the standard pattern for nature SCH, PDF 29-0712 is the standard pattern for ferrihydrite).

et al., 2021; Zhang P. et al., 2021; Chen et al., 2023). Furthermore, MR-1 and SRB consumed significant amounts of $H^+$ during metabolism (Bose et al., 2009; Zhang Z. et al., 2022), thereby increasing the system's pH (Figure 6C). The higher pH promotes -OH complexation with As(III) on the surface of SCH, facilitating the adsorption of As(III) (Wang X. et al., 2023). The presence of EPS on the surface of SCH was confirmed by FTIR results (Figure 7), which showed a series of distinctive new peaks in the infrared spectrum at 1,250–1707 $cm^{-1}$ after the reaction, corresponding to the characteristic peaks of EPS (Eboigbodin and Biggs, 2008).

The mineral composition of M-SCH and Y-SCH in the MR-1 system showed negligible changes compared to the pre-reaction state (Figure 8A). Previous studies indicated that Fe(II) can promote the reductive dissolution and transformation of SCH (Fan et al., 2019; Fan et al., 2023). Remarkably, despite the considerable Fe(II) content in the MR-1 system (Figure 6A), no discernible mineral transformation of SCH was observed. This can be attributed to the adsorption of EPS produced by MR-1 onto the SCH surface. The presence of EPS not only enhanced the adsorption of As(III) but also occupied active sites, impeding electron transfer between Fe(II) and Fe(III) on the SCH surface (Yan et al., 2021; Wang Q. et al., 2023). This decelerated the mineral transformation process. Additionally, although the metabolic activity of MR-1 elevated the system's pH (Figure 6C), the pH of the MR-1 system remained below the $pH_{-pcz}$ of synthetic SCH, which is approximately 7 (Jönsson et al., 2005). Consequently, the SCH surface was positively charged, hindering the adsorption of Fe(II) due to electrostatic repulsion. As a result, electron transfer from Fe(II) to SCH was weakened, further retarding the mineral transformation process. These two factors collectively explain the absence of noticeable mineral transformation of SCH in the MR-1 system.

Different from the MR-1 system, a peak at approximately 2-theta = 30.5° was observed in the SRB system after the reaction (Figure 8B). This newly observed peak is recognized as the characteristic peak of As(III)-bearing ferrihydrite generated within the system (the specific identification process of As(III)-bearing ferrihydrite is discussed in details in section 3.3). Similar phenomena have also been observed in the reductive dissolution

process of As-loaded SCH in the presence of $S^{2-}$ (Zhang et al., 2016). The transformation of SCH to As(III)-bearing ferrihydrite occurred only in the SRB system due to the considerably higher concentration of Fe(III) compared to the MR-1 system (Figure 6A). $S^{2-}$ generated by SRB exhibited a more pronounced reductive dissolution ability towards SCH compared to the Fe(II) produced by MR-1, resulting in a higher Fe(III) concentration in the SRB system (Poulton et al., 2004). However, the reduction ability of SRB towards Fe(III) is weaker than that of MR-1, leading to a higher proportion of Fe(III) in the SRB system (Figure 6A) (Zhang Y. et al., 2021). Under SRB mediation, the Fe(III) concentrations in the M-SCH and Y-SCH systems reached 11.57 mg/L and 9.39 mg/L, respectively, with pH values of 5.95 and 5.84 (Figures 6A–C). This concentration of Fe(III) and pH environment is highly favorable for the formation of ferrihydrite (Stumm and Morgan, 2013; Weatherill et al., 2016). However, the characteristic peaks of ferrihydrite on the XRD are not prominent (Figure 8B), which may be due to the inhibition of ferrihydrite formation in the SRB-mediated reducing environment (Cornell and Schwertmann, 2003; Stumm and Morgan, 2013).

Although no significant transformation of SCH occurred during the microbial influence experiment, both M-SCH and Y-SCH exhibited reductive dissolution in the presence of MR-1 and SRB. Additionally, the formation of As(III)-bearing ferrihydrite was observed in the SRB systems. The low crystallinity and poor stability of As(III)-bearing ferrihydrite, combined with the potential mineral transformation of SCH due to prolonged exposure to MR-1 and SRB, raise concerns regarding the release of As(III). Therefore, further investigations into the long-term stability and risks associated with the secondary release of SCH and As(III)-bearing ferrihydrite under the influence of MR-1 and SRB are warranted.

## 4 Conclusion

This study is the first to investigate the effects of MR-1 and SRB on the adsorption of As(III) by two optimized SCHs. Additionally, the generation and transformation of As(III)-bearing ferrihydrite were observed during the short-term adsorption process. During the interaction between As(III) and SCH, As(III) was not consistently oxidized to As(V). Meanwhile, SCH released significant amounts of $SO_4^{2-}$ and Fe(III), creating favorable conditions for the formation of As(III)-bearing ferrihydrite. In contrast to long-term experiments where SCH directly transformed into goethite, the As(III)-bearing ferrihydrite observed in this study likely represents an intermediate stage in the transformation of SCH into goethite. Furthermore, the $KMnO_4$ oxidation and ethanol modification methods effectively enhanced the physical adsorption capacity of SCH for As(III) by increasing its specific surface area and porosity. Physical adsorption played a leading role in the adsorption of As(III) by M-SCH and Y-SCH. Both FeRB and SRB enhanced the adsorption capacity of SCH for As(III), with SRB exerting a more substantial impact on SCH's phase transformation compared to FeRB. The EPS secreted by MR-1, adsorbed on the SCH surface, promoted surface complexation with As(III) while impeding electron transfer between Fe(II) and Fe(III), thereby decelerating the mineral transformation process. In the SRB system, the high concentration of Fe(III) and near-neutral pH favored the generation of As(III)-bearing ferrihydrite. This study provides new insights into the interfacial behavior and mechanism of As(III) on SCH, offering a scientific basis for advancing the practical application of SCH in As(III) pollution treatment.

## Data availability statement

The original contributions presented in the study are included in the article/Supplementary Material, further inquiries can be directed to the corresponding authors.

## Author contributions

HL: Writing–original draft, Visualization, Software, Methodology, Formal Analysis, Data curation, Conceptualization. WS: Writing–original draft, Formal Analysis, Data curation. ZL: Writing–review and editing, Validation, Software, Formal Analysis. WW: Writing–review and editing, Validation, Conceptualization. JH: Writing–review and editing, Supervision, Funding acquisition, Conceptualization. CL: Writing–review and editing, Validation, Supervision, Funding acquisition, Conceptualization.

## Funding

The author(s) declare that financial support was received for the research, authorship, and/or publication of this article. This work is supported by National Natural Science Foundation of China (Nos. 42167028, 32160299), Young Scientific and Technological Leading Talent Program of Inner Mongolia (NJYT2022092).

## Conflict of interest

The authors declare that the research was conducted in the absence of any commercial or financial relationships that could be construed as a potential conflict of interest.

## Publisher's note



## Supplementary material

The Supplementary Material for this article can be found online at: https://www.frontiersin.org/articles/10.3389/fenvs.2024.1482113/full#supplementary-material

# References


Ahmed, K. M., Bhattacharya, P., Hasan, M. A., Akhter, S. H., Alam, S. M., Bhuyian, M. H., et al. (2004). Arsenic enrichment in groundwater of the alluvial aquifers in Bangladesh: an overview. *Appl. Geochem.* 19 (2), 181–200. doi:10.1016/j.apgeochem.2003.09.006

Albadarin, A. B., Mangwandi, C., Al-Muhtaseb, A. a.H., Walker, G. M., Allen, S. J., and Ahmad, M. N. M. (2012). Kinetic and thermodynamics of chromium ions adsorption onto low-cost dolomite adsorbent. *Chem. Eng. J.* 179, 193–202. doi:10.1016/j.cej.2011.10.080

Alkan, M., Demirbaş, Ö., Çelikçapa, S., and Doğan, M. (2004). Sorption of acid red 57 from aqueous solution onto sepiolite. *J. HazardousMaterials* 116 (1-2), 135–145. doi:10.1016/j.jhazmat.2004.08.003

Antelo, J., Fiol, S., Gondar, D., López, R., and Arce, F. (2012). Comparison of arsenate, chromate and molybdate binding on schwertmannite: surface adsorption vs anion-exchange. *J. Colloid Interface Sci.* 386 (1), 338–343. doi:10.1016/j.jcis.2012.07.008

Bigham, J., Carlson, L., and Murad, E. (1994). Schwertmannite, a new iron oxyhydroxysulphate from Pyhäsalmi, Finland, and other localities. *Mineral. Mag.* 58 (393), 641–648. doi:10.1180/minmag.1994.058.393.14

Bose, S., Hochella Jr, M. F., Gorby, Y. A., Kennedy, D. W., McCready, D. E., Madden, A. S., et al. (2009). Bioreduction of hematite nanoparticles by the dissimilatory iron reducing bacterium Shewanella oneidensis MR-1. *Geochimica Cosmochimica Acta* 73 (4), 962–976. doi:10.1016/j.gca.2008.11.031

Brülls, M., Folestad, S., Sparén, A., Rasmuson, A., and Salomonsson, J. (2007). Applying spectral peak area analysis in near-infrared spectroscopy moisture assays. *J. Pharm. Biomed. Analysis* 44 (1), 127–136. doi:10.1016/j.jpba.2007.02.013

Burton, E. D., Bush, R. T., Johnston, S. G., Watling, K. M., Hocking, R. K., Sullivan, L. A., et al. (2009). Sorption of arsenic (V) and arsenic (III) to schwertmannite. *Environ. Sci. and Technol.* 43 (24), 9202–9207. doi:10.1021/es902461x

Burton, E. D., Bush, R. T., Sullivan, L. A., and Mitchell, D. R. (2008). Schwertmannite transformation to goethite via the Fe (II) pathway: reaction rates and implications for iron–sulfide formation. *Geochimica Cosmochimica Acta* 72 (18), 4551–4564. doi:10.1016/j.gca.2008.06.019

Cao, Q., Chen, C., Li, K., Sun, T., Shen, Z., and Jia, J. (2021). Arsenic (V) removal behavior of schwertmannite synthesized by $KMnO_4$ rapid oxidation with high adsorption capacity and Fe utilization. *Chemosphere* 264, 128398. doi:10.1016/j.chemosphere.2020.128398

Carrero, S., Fernandez-Martinez, A., Pérez-López, R., Poulain, A., Salas-Colera, E., and Nieto, J. M. (2017). Arsenate and selenate scavenging by basaluminite: insights into the reactivity of aluminum phases in acid mine drainage. *Environ. Sci. and Technol.* 51 (1), 28–37. doi:10.1021/acs.est.6b03315

Chen, J., Qu, C., Lu, M., Zhang, M., Wu, Y., Gao, C., et al. (2023). Extracellular polymeric substances and mineral interfacial reactions control the simultaneous immobilization and reduction of arsenic (As (V)). *J. Hazard. Mater.* 456, 131651. doi:10.1016/j.jhazmat.2023.131651

Chen, J., and Rosen, B. P. (2020). The arsenic methylation cycle: how microbial communities adapted methylarsenicals for use as weapons in the continuing war for dominance. *Front. Environ. Sci.* 8, 43. doi:10.3389/fenvs.2020.00043

Chen, M., Lu, G., Wu, J., Sun, J., Yang, C., Xie, Y., et al. (2020). Acidity and metallic elements release from AMD-affected river sediments: effect of AMD standstill and dilution. *Environ. Res.* 186, 109490. doi:10.1016/j.envres.2020.109490

Chen, Q., Cohen, D. R., Andersen, M. S., Robertson, A. M., and Jones, D. R. (2022). Stability and trace element composition of natural schwertmannite precipitated from acid mine drainage. *Appl. Geochem.* 143, 105370. doi:10.1016/j.apgeochem.2022.105370

Cornell, R. M., and Schwertmann, U. (2003). *The iron oxides: structure, properties, reactions, occurrences, and uses*. Wiley-vch Weinheim.

Dou, X., Mohan, D., and Pittman Jr, C. U. (2013). Arsenate adsorption on three types of granular schwertmannite. *Water Res.* 47 (9), 2938–2948. doi:10.1016/j.watres.2013.01.035

Eboigbodin, K. E., and Biggs, C. A. (2008). Characterization of the extracellular polymeric substances produced by *Escherichia coli* using infrared spectroscopic, proteomic, and aggregation studies. *Biomacromolecules* 9 (2), 686–695. doi:10.1021/bm701043c

Fan, C., Guo, C., Chen, W., Lu, G., Shen, Y., and Dang, Z. (2023). Fe (II)-mediated transformation of schwertmannite associated with calcium from acid mine drainage treatment. *J. Environ. Sci.* 126, 612–620. doi:10.1016/j.jes.2022.05.044

Fan, C., Guo, C., Zeng, Y., Tu, Z., Ji, Y., Reinfelder, J. R., et al. (2019). The behavior of chromium and arsenic associated with redox transformation of schwertmannite in AMD environment. *Chemosphere* 222, 945–953. doi:10.1016/j.chemosphere.2019.01.142

Gan, M., Zheng, Z., Sun, S., Zhu, J., and Liu, X. (2015). The influence of aluminum chloride on biosynthetic schwertmannite and Cu (II)/Cr (VI) adsorption. *RSC Adv.* 5 (114), 94500–94512. doi:10.1039/c5ra17316g

Gao, M., Su, Y., Gao, J., Zhong, X., Li, H., Wang, H., et al. (2022). Arsenic speciation transformation in soils with high geological background: new insights from the governing role of Fe. *Chemosphere* 302, 134860. doi:10.1016/j.chemosphere.2022.134860

Gulledge, J. H., and O'Connor, J. T. (1973). Removal of arsenic (V) from water by adsorption on aluminum and ferric hydroxides. *Journal-American Water Works Assoc.* 65 (8), 548–552. doi:10.1002/j.1551-8833.1973.tb01893.x

Guo, L., Ye, P., Wang, J., Fu, F., and Wu, Z. (2015). Three-dimensional $Fe_3O_4$-graphene macroscopic composites for arsenic and arsenate removal. *J. Hazard. Mater.* 298, 28–35. doi:10.1016/j.jhazmat.2015.05.011

Ho, Y.-S., and McKay, G. (1999). Pseudo-second order model for sorption processes. *Process Biochem.* 34 (5), 451–465. doi:10.1016/s0032-9592(98)00112-5

Jia, H., Zhang, Z., Sun, S., Li, Y., Song, Z., Huang, H., et al. (2024). Multifunctional schwertmannite-loaded nano zero-valent iron for highly efficient removal of hexavalent chrome from aqueous solution. *J. Environ. Chem. Eng.* 12 (3), 112696. doi:10.1016/j.jece.2024.112696

Johnston, S. G., Keene, A. F., Burton, E. D., Bush, R. T., and Sullivan, L. A. (2011). Iron and arsenic cycling in intertidal surface sediments during wetland remediation. *Environ. Sci. and Technol.* 45 (6), 2179–2185. doi:10.1021/es103403n

Jönsson, J., Persson, P., Sjöberg, S., and Lövgren, L. (2005). Schwertmannite precipitated from acid mine drainage: phase transformation, sulphate release and surface properties. *Appl. Geochem.* 20 (1), 179–191. doi:10.1016/j.apgeochem.2004.04.008

Ke, C., Guo, C., Zhang, S., Deng, Y., Li, X., Li, Y., et al. (2023). Microbial reduction of schwertmannite by co-cultured iron-and sulfate-reducing bacteria. *Sci. Total Environ.* 861, 160551. doi:10.1016/j.scitotenv.2022.160551

Lee, S. Y., Kim, Y., Kang, S. A., Chang, B., Hur, H., and Lee, Y. J. (2023). Characterization of arsenic (III and V) adsorption on natural schwertmannite formed in acid coal mine drainage: batch studies and spectroscopic observations. *J. Environ. Chem. Eng.* 11 (1), 109170. doi:10.1016/j.jece.2022.109170

Li, H., Wang, J., Zhao, B., Gao, M., Shi, W., Zhou, H., et al. (2018). The role of major functional groups: multi-evidence from the binding experiments of heavy metals on natural fulvic acids extracted from lake sediments. *Ecotoxicol. Environ. Saf.* 162, 514–520. doi:10.1016/j.ecoenv.2018.07.038

Li, X., Guo, C., Jin, X., He, C., Yao, Q., Lu, G., et al. (2021). Mechanisms of Cr (VI) adsorption on schwertmannite under environmental disturbance: changes in surface complex structures. *J. Hazard. Mater.* 416, 125781. doi:10.1016/j.jhazmat.2021.125781

Li, Y., and Wei, M. (2022). Evaluation on adsorption capacity of low organic matter soil for hydrophobic organic pollutant. *J. Environ. Chem. Eng.* 10 (3), 107561. doi:10.1016/j.jece.2022.107561

Ma, W.-J., Zhang, J.-T., Wang, Y., Li, G.-F., Wu, X.-X., Yao, Y.-X., et al. (2021). Extracellular polymeric substances excreted by anammox sludge act as a barrier for as (III) invasion: binding property and interaction mechanism. *Chemosphere* 278, 130414. doi:10.1016/j.chemosphere.2021.130414

Morin, G., Juillot, F., Casiot, C., Bruneel, O., Personné, J.-C., Elbaz-Poulichet, F., et al. (2003). Bacterial formation of tooeleite and mixed arsenic (III) or arsenic (V)– iron (III) gels in the Carnoulès acid mine drainage, France. A XANES, XRD, and SEM study. *Environ. Sci. and Technol.* 37 (9), 1705–1712. doi:10.1021/es025688p

Naren, G., Ohashi, H., Bai, S., Yonezu, K., and Yokoyama, T. (2023). Uptake mechanism of silicic acid by schwertmannite and its stabilization. *J. Environ. Chem. Eng.* 11 (6), 111136. doi:10.1016/j.jece.2023.111136

Oremland, R. S., and Stolz, J. F. (2003). The ecology of arsenic. *Science* 300 (5621), 939–944. doi:10.1126/science.1081903

Oscarson, D., Huang, P., and Liaw, W. (1980). *The oxidation of arsenite by aquatic sediments*. Wiley Online Library.

Paikaray, S., Göttlicher, J., and Peiffer, S. (2011). Removal of as (III) from acidic waters using schwertmannite: surface speciation and effect of synthesis pathway. *Chem. Geol.* 283 (3-4), 134–142. doi:10.1016/j.chemgeo.2010.08.011

Paikaray, S., Göttlicher, J., and Peiffer, S. (2012). As (III) retention kinetics, equilibrium and redox stability on biosynthesized schwertmannite and its fate and control on schwertmannite stability on acidic (pH 3.0) aqueous exposure. *Chemosphere* 86 (6), 557–564. doi:10.1016/j.chemosphere.2011.07.055

Peak, D., Ford, R. G., and Sparks, D. L. (1999). An *in situ* ATR-FTIR investigation of sulfate bonding mechanisms on goethite. *J. Colloid Interface Sci.* 218 (1), 289–299. doi:10.1006/jcis.1999.6405

Pi, K., Wang, Y., Xie, X., Su, C., Ma, T., Li, J., et al. (2015). Hydrogeochemistry of co-occurring geogenic arsenic, fluoride and iodine in groundwater at Datong Basin, northern China. *J. Hazard. Mater.* 300, 652–661. doi:10.1016/j.jhazmat.2015.07.080

Poulton, S. W., Krom, M. D., and Raiswell, R. (2004). A revised scheme for the reactivity of iron (oxyhydr) oxide minerals towards dissolved sulfide. *Geochimica Cosmochimica Acta* 68 (18), 3703–3715. doi:10.1016/j.gca.2004.03.012

Regenspurg, S., Brand, A., and Peiffer, S. (2004). Formation and stability of schwertmannite in acidic mining lakes 1 1Associate editor: C. M. Eggleston. *Geochimica Cosmochimica Acta* 68 (6), 1185–1197. doi:10.1016/j.gca.2003.07.015

Schoepfer, V. A., and Burton, E. D. (2021). Schwertmannite: a review of its occurrence, formation, structure, stability and interactions with oxyanions. *Earth-Science Rev.* 221, 103811. doi:10.1016/j.earscirev.2021.103811

Shi, W., Song, W., Zheng, J., Luo, Y., Qile, G., Lü, S., et al. (2021). Factors and pathways regulating the release and transformation of arsenic mediated by reduction processes of dissimilated iron and sulfate. *Sci. Total Environ.* 768, 144697. doi:10.1016/j.scitotenv.2020.144697

Song, J., Jia, S.-Y., Ren, H.-T., Wu, S.-H., and Han, X. (2015). Application of a high-surface-area schwertmannite in the removal of arsenate and arsenite. *Int. J. Environ. Sci. Technol.* 12, 1559–1568. doi:10.1007/s13762-014-0528-9

Stumm, W., and Morgan, J. J. (2013). *Aquatic chemistry: chemical equilibria and rates in natural waters*. John Wiley and Sons.

Takaya, Y., Kadokura, M., Kato, T., and Tokoro, C. (2021). Removal mechanisms of arsenite by coprecipitation with ferrihydrite. *J. Environ. Chem. Eng.* 9 (5), 105819. doi:10.1016/j.jece.2021.105819

Thakur, N., and Armstrong, D. W. (2021). Arsenic sequestration by iron oxide coated geopolymer microspheres. *J. Clean. Prod.* 291, 125931. doi:10.1016/j.jclepro.2021.125931

Tian, Y., Liu, F., Sun, B., Tong, Z., Fu, P., Zhang, J., et al. (2023). Efficient removal of doxycycline using Schwertmannite as a heterogeneous Fenton-like catalyst over a wide pH range. *J. Environ. Chem. Eng.* 11 (2), 109441. doi:10.1016/j.jece.2023.109441

Vithana, C. L., Sullivan, L. A., Burton, E. D., and Bush, R. T. (2014). Liberation of acidity and arsenic from schwertmannite: effect of fulvic acid. *Chem. Geol.* 372, 1–11. doi:10.1016/j.chemgeo.2014.02.012

Vithana, C. L., Sullivan, L. A., Burton, E. D., and Bush, R. T. (2015). Stability of schwertmannite and jarosite in an acidic landscape: prolonged field incubation. *Geoderma* 239, 47–57. doi:10.1016/j.geoderma.2014.09.022

Wang, Q., Wang, J., Wang, X., Kumar, N., Pan, Z., Peiffer, S., et al. (2023a). Transformations of ferrihydrite–extracellular polymeric substance coprecipitates driven by dissolved sulfide: interrelated effects of carbon and sulfur loadings. *Environ. Sci. and Technol.* 57 (10), 4342–4353. doi:10.1021/acs.est.2c06921

Wang, X., Fu, J., Dong, Y., Wang, L., and Zhou, L. (2023b). Alkaline modification on schwertmannite promoted the simultaneous immobilization of arsenite and cadmium. *Chem. Eng. J.* 454, 140236. doi:10.1016/j.cej.2022.140236

Wang, X. M., Fu, J. R., Dong, Y., Wang, L. J., and Zhou, L. X. (2023c). Alkaline modification on schwertmannite promoted the simultaneous immobilization of arsenite and cadmium. *Chem. Eng. J.* 454, 140236. doi:10.1016/j.cej.2022.140236

Wang, Y., Gao, M., Huang, W., Wang, T., and Liu, Y. (2020). Effects of extreme pH conditions on the stability of as (V)-bearing schwertmannite. *Chemosphere* 251, 126427. doi:10.1016/j.chemosphere.2020.126427

Weatherill, J. S., Morris, K., Bots, P., Stawski, T. M., Janssen, A., Abrahamsen, L., et al. (2016). Ferrihydrite formation: the role of $Fe^{13}$ Keggin clusters. *Environ. Sci. and Technol.* 50 (17), 9333–9342. doi:10.1021/acs.est.6b02481

Wieser, M., Traxl, R., Unterberger, S., and Lackner, R. (2022). Assessment of aging state of bitumen based on peak-area evaluation in infrared spectroscopy: influence of data processing and modeling. *Constr. Build. Mater.* 326, 126798. doi:10.1016/j.conbuildmat.2022.126798

Xie, Y., Lu, G., Ye, H., Yang, C., Xia, D., Yi, X., et al. (2017). Fulvic acid induced the liberation of chromium from $CrO_4^{2-}$-substituted schwertmannite. *Chem. Geol.* 475, 52–61. doi:10.1016/j.chemgeo.2017.10.031

Yan, W., Guo, W., Wang, L., and Jing, C. (2021). Extracellular polymeric substances from Shewanella oneidensis MR-1 biofilms mediate the transformation of Ferrihydrite. *Sci. Total Environ.* 784, 147245. doi:10.1016/j.scitotenv.2021.147245

Yang, Z., Bai, L., Su, S., Wang, Y., Wu, C., Zeng, X., et al. (2021). Stability of Fe–As composites formed with as (V) and aged ferrihydrite. *J. Environ. Sci.* 100, 43–50. doi:10.1016/j.jes.2020.07.015

Ying, H., Feng, X., Zhu, M., Lanson, B., Liu, F., and Wang, X. (2020). Formation and transformation of schwertmannite through direct $Fe^{3+}$ hydrolysis under various geochemical conditions. *Environ. Sci. Nano* 7 (8), 2385–2398. doi:10.1039/d0en00252f

Yuan, Z., Zhang, G., Ma, X., Yu, L., Wang, X., Wang, S., et al. (2021). A combined abiotic oxidation-precipitation process for rapid as removal from high-As (III)-Mn (II) acid mine drainage and low As-leaching solid products. *J. Hazard. Mater.* 401, 123360. doi:10.1016/j.jhazmat.2020.123360

Zhang, D., Wu, S., Wei, Y., and Zhou, L. (2022a). Schwertmannite modified with ethanol: a simple and feasible method for improving as (III) adsorption capacity. *J. Environ. Chem. Eng.* 10 (3), 107412. doi:10.1016/j.jece.2022.107412

Zhang, P., Xu, X.-Y., Zhang, X.-L., Zou, K., Liu, B.-Z., Qing, T.-P., et al. (2021a). Nanoparticles-EPS corona increases the accumulation of heavy metals and biotoxicity of nanoparticles. *J. Hazard. Mater.* 409, 124526. doi:10.1016/j.jhazmat.2020.124526

Zhang, S.-L., Jia, S.-Y., Yu, B., Liu, Y., Wu, S.-H., and Han, X. (2016). Sulfidization of as (V)-containing schwertmannite and its impact on arsenic mobilization. *Chem. Geol.* 420, 270–279. doi:10.1016/j.chemgeo.2015.11.020

Zhang, Y., Zhu, Z., Liao, Y., Dang, Z., and Guo, C. (2021b). Effects of Fe (II) source on the formation and reduction rate of biosynthetic mackinawite: biosynthesis process and removal of Cr (VI). *Chem. Eng. J.* 421, 129723. doi:10.1016/j.cej.2021.129723

Zhang, Z., Zhang, C., Yang, Y., Zhang, Z., Tang, Y., Su, P., et al. (2022b). A review of sulfate-reducing bacteria: metabolism, influencing factors and application in wastewater treatment. *J. Clean. Prod.* 376, 134109. doi:10.1016/j.jclepro.2022.134109

Zhao, D., Sheng, G., Hu, J., Chen, C., and Wang, X. (2011a). The adsorption of Pb (II) on $Mg_2Al$ layered double hydroxide. *Chem. Eng. J.* 171 (1), 167–174. doi:10.1016/j.cej.2011.03.082

Zhao, Z., Jia, Y., Xu, L., and Zhao, S. (2011b). Adsorption and heterogeneous oxidation of as (III) on ferrihydrite. *Water Res.* 45 (19), 6496–6504. doi:10.1016/j.watres.2011.09.051